Supplement

Methods

Molecular Dynamics

Details on MD setup protocol beyond what is in the Methods section are given below. The SHAKE algorithm was used to constrain covalent bonds containing hydrogen atoms, thereby allowing a 2 fs time-step to be used for all trials. Periodic boundary conditions (PBC) were applied for both minimization and dynamic steps. Minimization was 1000 steps, during which the protein was held fixed with restraints of 500.0 kcal/ $(mol\AA^2)$. Steepest descent and conjugate gradient optimization methods were used. Another minimization was performed for 5000 steps, the only difference being that all atoms were movable. The Berendsen thermostat and barostat (for constant pressure simulations) were used, and non-bonding interactions (10 $\AA$ cut-off) were calculated using particle mesh Ewald (PME) theory. The AMBER BELLY command was used during the first equilibration (NVT) to keep the protein fixed while the water molecules and counter ions were heated from 0 to 300 K. This heating took place over the course of 0.08 ns and a temperature of 300 K was maintained for 0.02 ns. Next, with all atoms movable, the entire system was heated from 0 to 300 K over the course of 0.4 ns and the temperature of 300 K was maintained for the remaining 0.1 ns. The final equilibration was run for 1 ns under NPT conditions (300 K and 1 bar). All atoms were movable and the pressure relaxation time was 2.0 ps. Atom velocities were randomly initialized for the production runs. The temperature of the system was maintained at 300 K throughout the production run. Similarly, the pressure was maintained at 1 bar with a 2.0 ps relaxation time. Genheden and Ryde[80] suggest one long 300 ns simulation or 20 short 400 ps simulations in order to obtain statistically significant/convergent data. We have performed three 100 ns simulations for each system, which adds up to the recommended time of 300 ns, while also giving the data even greater independence than one 300 ns simulation. Genheden and Ryde[80] suggest a statistical decorrelation time of 2-7 ps and state that simulations in

MM energy calculations should be performed accordingly. Our MM energy analyses were run for 100 one ns time points, which exceeds the speculated decorrelation time by three orders of magnitude. Errors within an MM energy simulation are fairly small. Standard errors for each energy value obtained hover around 1-2%, which means our 95% confidence interval for the energy value is approximately 2-4% of the obtained value (since n = 100, we assume a normal distribution of independent events (because our time-steps exceed the decorrelation time), and the t-value for a 95% confidence interval is 1.96).

Models of ion hydration

The GB model of hydration energy is given by

$$\Delta G_{GB} = \frac{z^2}{r} \left(\frac{e^2 N_a}{2 \cdot 4\pi\epsilon_0} \right) \left(1 - \frac{1}{\epsilon_r} \right) \tag{S1}$$

and describes the process of moving an ion of fixed radius r and charge ze_0 (where z is the charge number from a medium of dielectric $\epsilon = 1$ to a polar medium of $\epsilon = 80$. The DH model accounts for the shielding of the electrostatic potential by a strongly mixed electrolyte solution

$$\Delta G_{DH} = \frac{z^2}{r(1 + \kappa r)} \left(\frac{e^2 N_a}{2 \cdot 4\pi\epsilon_0} \right) \left(1 - \frac{1}{\epsilon_r} \right) \tag{S2}$$

where κ reflects the inverse Debye length (see Eq. S10), a measure of the electrostatic shielding due to a strong electrolyte solution.[81] In both of the above equations, N_a is Avogadro's constant and ϵ_r is the dielectric of the solvent and ϵ_0 is the permittivity of free space.

Mean spherical approximation theory

We summarize here the core MSA equations following the derivation from Nonner et al.[31] The Helmholtz free energy, ΔA, of an electrolyte solution can be partitioned into ideal and

excess components

$$\Delta A = \Delta A_{ideal} + \Delta A_{excess} \tag{S3}$$

$$= \Delta A_{ideal} + \Delta A_{HS} + \Delta A_{ES} \tag{S4}$$

$$\tag{S5}$$

MSA further partitions the excess free energy into hard sphere and electrostatic components (ΔA_{HS} and ΔA_{ES}), respectively. The hard sphere component approximates the entropy from a system of ions with fixed, non-zero radii. In a similar vein, the electrostatic component describes charged interactions between ions with non-vanishing radii. Comprising the electrostatic free energy are enthalpic and entropic terms as represented by

$$\Delta E_{ES} = -\frac{\lambda_b}{\beta} \sum_i \rho_i \left(\frac{z_i^2}{\sigma_i + 1/\Gamma} + \frac{z_i \eta \sigma_i/\Gamma}{\sigma + 1/\Gamma} \right) \tag{S6}$$

and

$$\Delta S_{ES} = -\frac{k_B}{3\pi} \Gamma^3 \tag{S7}$$

In these equations, ρ_i, z_i, and σ_i are the concentration, charge, and radius of ion i. The thermal energy is represented by $\beta = 1/k_b T$, where k_b is the gas constant and T is temperature. λ_b represents the Bjerrum length defined as

$$\lambda_b = \frac{e^2}{4\pi\epsilon_0\epsilon_r k_b T} \tag{S8}$$

where e is the fundamental electron charge, while ϵ_0 and ϵ_r are the vacuum and relative permittivities, respectively. For context, λ_b is approximately 0.7 nm at T=300 K in a medium of $\epsilon_r \approx 80$.

An important development in MSA theory is its description of shielded electrostatic interactions, which is encapsulated in the Γ term. Γ is implicitly determined through the expression

$$\Gamma^2 = \pi\lambda_b \sum_i \rho_i \left[\frac{z_i - \eta\sigma_i^2}{1 + \Gamma\sigma_i}\right]^2 \tag{S9}$$

In essence, the assumption of finite radii reduces the capacity for mobile ions to shield electrostatic interactions; this contrasts with traditional electrolyte models, such as the Debye-Huckel model, that assume infinitesimally small ions. It is easily shown in the limit that $\sigma_i \to 0$ that Eq. S9 is equivalent to the inverse Debye length, κ from Debye-Huckel theory:

$$\pi^{-1}\Gamma^2 \to \lambda_b \sum_i \rho_i z_i^2 = \kappa^2/4 \tag{S10}$$

Lastly, the contribution of unequal ion sizes is quantified as η, which is in part dependent on the free volume not occupied by hard spheres, Δ. These terms are estimated through

$$\eta = \frac{\pi}{2\Omega\Delta} \sum_k \frac{\rho_k \sigma_k z_k}{1 + \Gamma\sigma_k} \tag{S11}$$

$$\Omega = 1 + \frac{\pi}{2\Delta} \sum_k \frac{\rho_k \sigma_k^3}{1 + \Gamma\sigma_k} \tag{S12}$$

$$\Delta = 1 - \frac{\pi}{6} \sum_k \rho_k \sigma_k^3 \tag{S13}$$

The excess chemical potential from hard-spheres is expressed as

$$\Delta\mu_i^{HS} = k_b T \left[\frac{3\xi_2\sigma_i + 3\xi_1\sigma_i^2}{\Delta} + \frac{9\xi_2^2\sigma_i^2}{2\Delta^2} + \xi_0\sigma_i^3(1 + \Delta\phi^{HS}) - ln\Delta\right] \tag{S14}$$

Where

$$\Delta\phi^{HS} = \frac{\xi_3}{\Delta} + \frac{3\xi_1\xi_2}{\xi_0\Delta^2} + \frac{3\xi_2^3}{\xi_0\Delta^3} \tag{S15}$$

and

$$\xi_n = \frac{\pi}{6} \sum_k \rho_k \sigma_k^n \tag{S16}$$

The excess chemical potentials for species i are obtained by differentiating the Helmholtz free energy by the ion's concentration

$$\Delta\mu_i = \frac{\partial}{\partial\rho_i}\Delta A \tag{S17}$$

$$\tag{S18}$$

The electrostatic contribution to excess chemical potential is:

$$\Delta\mu_i^{ES} = -\frac{\lambda_b}{\beta}\left[\frac{\Gamma z_i^2}{1+\Gamma\sigma_i} + \eta\sigma_i\left(\frac{2z_i - \eta\sigma_i^2}{1+\Gamma\sigma_i} + \frac{\eta\sigma_i^2}{3}\right)\right] \tag{S19}$$

Thus, the free energy from the hard-sphere interactions is

$$\Delta A^{HS} = -T\Delta S^{HS} = \sum_i \rho_i \Delta\mu_i^{HS} - \Delta\phi^{HS}\beta\sum_i \rho_i \tag{S20}$$

The number density of ion i, ρ_i is obtained as

$$k_B T \ln \rho_i = k_B T \ln \rho_{0,i} + \mu_{0,i}^{ex} - z_i e_0 \Psi - \mu_i^{ex} \tag{S21}$$

We note that Ψ could also be obtained directly via numerical solution of the Poisson equation (refer to[82]), given appropriate fixed and mobile charge distributions

$$-\epsilon_0 \nabla \cdot (\epsilon(x)\nabla\Psi(x)) = e_0 \sum_i z_i \rho_i(x) \tag{S22}$$

MSA parameter selection

Dielectric constant   As discussed previously, a filter dielectric constant of 25.0 was chosen for the MSA model of the PV system. Our rationale is tied to Fig. S13, which shows excess chemical potential values plotted against a wide range of dielectric constants and filter volumes. Per the data in Table 1 and our simulations of the EF-hand domains, reasonable

volumes to use in MSA are in the 0.4 to 0.7 nm^3 range. Our choice of dielectric constant was based on the finding that chemical potentials within the filter were largely indistinguishable for $\epsilon = 20$ to $\epsilon = 30$. For $\epsilon > 30$, the model predicted thermodynamically unfavorable binding ($\mu > 0$), whereas the model was unstable for constants below 20.

Ion radii A variety of cationic radii have been proposed for use with molecular and mean-field simulations of electrolytes. In the Nonner study,[32] radii were derived from.[63] Modified radii were later proposed[83] in order to reconcile inconsistencies between hydration energies for cations and predictions from GB theory. More recently, we provided revised ionic radii for a finite-sized ion PB model, in order to better reconcile cation distributions near phospholipid membranes.[84] Similar revisions of effective radii and interaction parameters for cations have been proposed for their interactions with explicit water solvents and proteins. Parameters from Roux et al. have been used for Ca^{2+} channels,[85] while Li-Merz more recently presented modifications that represent a compromise between solvent coordination number and hydration energies.[17] Given the similar chemical potentials predicted for Mg^{2+} and Ca^{2+} in the main body of the manuscript, slight variations in the cation radii do not appear to influence the MSA results to a large degree.

Results

Glutamic acid rotamer positions

We initialized our β-PV Mg^{2+}-bound EF-hand coordinating residue rotamers based on the EF-hand configuration of the Mg^{2+}-bound pike PV NMR-derived structure (PDB code, 4PAL[9]). According to Grabarek,[8] the glutamic acid in the twelfth position rotates $120\,^{\circ}$ from the Ca^{2+}-bound rotamer to the Mg^{2+}-bound rotamer in order to transition from a bidentate to a monodentate interaction. Thus, in order to generate the Mg^{2+}-bound configuration for both the L_{CD} and L_{EF} (since they have never been determined experimentally), we decided to use the Ca^{2+}-bound conformation (PDB code, 1RRO[34]), replace the Ca^{2+}

with Mg^{2+} and rotate the E62 and E101 rotamers of the L_{CD} and L_{EF} respectively. Using Chimera software,[86] twenty-seven possible rotamers for each of the glutamic acid residues were generated with the Dunbrack library[87] and ranked according to likelihood. The first rotamer, in each case, was closest to the crystal structure with χ angles of $-70.8°$, $176.1°$, and $-3.7°$ for E62 and $-70.6°$, $174.9°$, and $-3.9°$ for E101. From the 27 rotamers generated for each glutamic acid, we selected the most probable one with rotation about the beta-carbon/gamma-carbon bond so that the new χ angles for E62 are $62.0°$, $-179.9°$, and $2.4°$, and $65.2°$, $-179.6°$, and $2.7°$ for E101. From here, we used the procedures outlined above to generate the solvated and neutralized protein system and to preform MD simulations. However, to ensure proper Mg^{2+}-coordination with the protein oxygens, we applied constraints during the simulations. In the second minimization step, the entire protein was movable except for the EF hands, which had a force constraint of 500.0 kcal/$(mol\mathring{A}^2)$, and E62 and E101, which have a force constraint of 5.0 kcal/$(mol\mathring{A}^2)$. For the equilibration steps, the entire protein and the Mg^{2+} are fixed with a constraint of 500.0 kcal/$(mol\mathring{A}^2)$ except E62 and E101, which have weak constraints of 5.0 kcal/$(mol\mathring{A}^2)$. Like the simulations in the main text, no constraints were applied during the production run (lasting at least 90 ns), which was conducted in triplicate.

The three different simulations produced three different patterns of Mg^{2+} coordination. In the first run, both the L_{CD} and L_{EF} showed that the glutamic acid in the twelfth position has a monodentate interaction with the Mg^{2+}. In the second run, E62 in the L_{CD} has the monodentate configuration, but E101 in the L_{EF} has a bidentate one. For the third run, both EF hands showed bidentate interactions between E62 and E101 and the Mg^{2+} hand. All three configurations were stable for the duration of the simulation. These results indicate that the monodentate interaction between Mg^{2+} and the glutamic acid in the twelfth position is not a stable one, and that the coordination between the two residues is flexible.

In order to quantify this flexibility, we calculated the RMSFs averaged over the three runs for each residue of the protein for the Ca^{2+}-bound and the two Mg^{2+}-bound cases –

one with the 4PAL rotamers and one with the Chimera software rotamers described above (Fig. S4). For the three cases, the average RMSF of the two Mg^{2+}-bound proteins is greater than that of the Ca^{2+}-bound one in the regions of residues 40-70, which includes the L_{CD}. The standard error of the Mg^{2+} cases calculated over the three simulations, however, is so large that it encompasses the Ca^{2+} -bound average from residues 40-45, 50-55, and 65-70. In the L_{CD} (residues 51-62), the RMSFs of the Ca^{2+} -bound case is statistically lower than those of the Mg^{2+}-bound cases; thus, the Ca^{2+} ion is more effective at stabilizing the L_{CD} than the Mg^{2+} ions. As for the L_{EF} (residues 90-101), the Mg^{2+}-bound case with the 4PAL rotamers has a larger RMSF than the other two cases; however, its error bars are so large, that the RMSFs of this simulation are not statistically different than the other ones. In general, across the entire protein, the standard error in the RMSFs is greater for the Mg^{2+}-bound case with 4PAL rotamers versus the Mg^{2+} -bound case with Chimera rotamers for the glutamic acids. The three simulations of the Mg^{2+}-bound cases with Chimera rotamers have lower RMSFs in the L_{EF} when Mg^{2+} interacts in a monodentate mode, which suggests that the structures with the Chimera rotamers are more stable than those with the 4PAL ones.

MSA validation

Fig. S10 shows our MSA calculations based on the reported parameters in Nonner et al.[88] for the L-type Ca^{2+} channel. First, we see that the excess chemical potential of Ca^{2+} for this given system begins at -4 kT and gradually decreases to -6 kT as $[Ca^{2+}]$ increases. Na^+, on the other hand, has positive chemical potential values, starting at 1 kT and approaching 0. Similarly, Cl^- has a positive chemical potential, beginning at 7 kT and dropping to and 5 kT as $[Ca^{2+}]$ is increased from 0.1 nM to 0.1 M.

The next subplot shows the ion density in the filter with respect to $[Ca^{2+}]$. Cl^- stays at 0 M, while Na^+ decreases from 17 M to 0 M as $[Ca^{2+}]$ in the filter rises from 0 M to 9 M. The final subplot in Fig. S10 shows the Donnan potential of the system as the bath $[Ca^{2+}]$ is

increased. The potential rises from -170 mV to 0 mV. This reflects the gradual decrease in the electrochemical gradient between the filter and the bath as more $CaCl_2$ is added to the bulk solution. All of these results are congruent with those in Nonner et al.,[88] thus giving us confidence in the mathematical precision of our calculations.

Our analysis of the breakdown of chemical potentials (see Fig. S12) follows. At roughly Ca^{2+}=0 ($[Ca^{2+}]$ = 0.1 nM), the excess potential of adding Ca^{2+} is favorable (-4 kT), while those of Cl^- and Na^+ are unfavorable at 7 and 1 kT, respectively. The unfavorable Cl^- binding can be readily attributed to the ion's considerable hard sphere penalty ($\approx$9 kT) that is only partially compensated by a modest electrostatic energy of -2. In the case of Na^+, a similar electrostatic energy of -2 kT is present, but its hard sphere penalty is significantly less (around 1 kT), leading to a less unfavorable overall chemical potential.

In contrast, Ca^{2+} has a hard sphere penalty similar to that of Na^+, but its divalent charge depresses the favorable electrostatic contributions to -8 kT. Gamma (and thus electrostatic energy) increases with concentration (see Nonner et al., 2000, eqs. 1-11). For hard sphere contributions, there are ξ terms used that depend on concentration. Also, as the ionic species of interest is excluded from the filter– or the probability of it being there decreases– the hard sphere interactions decrease. The results from the MSA validation calculations, which are presented in Fig. S10, are in close agreement with the results from Figure 4 in Nonner et al.[88] As expected, Ca^{2+} has the lowest chemical potential for all concentrations of $CaCl_2$, implying the binding site favors Ca^{2+} at the appropriate bath concentration.

Sensitivity of MSA predictions to coordination number and radii.

In Fig. S1, we present the hard-sphere contributions to the excess chemical potential of Ca^{2+} (A, C, and E) and Mg^{2+} (B, D, and F) across a filter volume range of 0.1 - 3.0 nm^3 and a filter dielectric constant range of 10-100. The number of chelating oxygens was fixed to 5 (A,B), 6 (C,D), or 7 (E,F) and $[Ca^{2+}]$ was held at 1 μM. Our results show that neither the number of chelating oxygens, nor the identity of the ion had a notable impact on the hard-sphere

contribution of the excess chemical potential. Furthermore, volume had a negligible impact after the filter was sufficiently large (> 0.6 nm^3). Finally, hard-sphere contributions to the excess chemical potential remained largely invariant with respect to dielectric constant for a given volume. The exceptions to this occurred only at the minima and maxima of the dielectric constant range.

Fig. S2 shows a similar plot for the electrostatic contribution to the excess chemical potential. We again observe that the trends in chemical potential values with respect to dielectric constant and volume are nearly identical between ions. We report the general trend that decreasing the dielectric constant value from that of bulk water (nearly 80) toward zero leads to more negative (favorable) electrostatic chemical potentials. However, in contrast to the hard-sphere contributions, we observe that the chemical potential for filter volumes below 1.2 nm^3 become less favorable for increasing carbonyl oxygen densities. These data indicate that although electrostatic interactions between the bound cation and the filter oxygens are favorable, there is a thermodynamic cost for increasing the oxygen density within narrow volumes.

Solvent accessible surface area

A common trend among Ca^{2+}-binding proteins (CBPs) is a reduction of surface area exposed to the solvent upon binding Ca^{2+}. This has been done by performing SASA calculations in order to compare the solvent exposure of hydrophobic residues in Ca^{2+}-bound, Mg^{2+}-bound, and apo PV. Our results in Fig. 5 suggest that both hydrophilic and hydrophobic SASA is reduced during cation binding. SASA is reduced to similar extents for both Mg^{2+} and Ca^{2+}.

Supplementary Figures
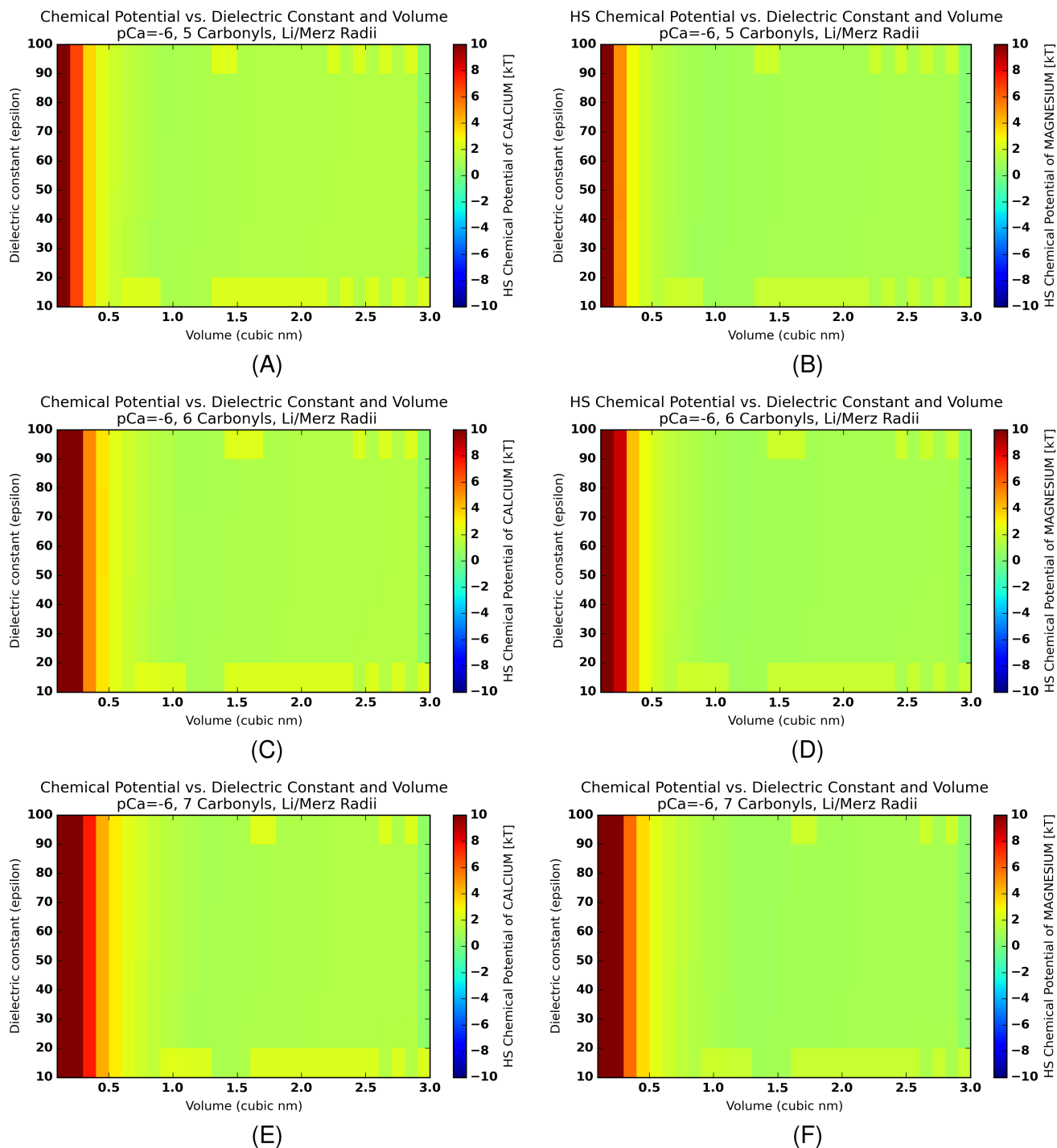
Figure S1: Hard-sphere contributions to the excess chemical potential of ionic species using radii from Li/Merz and PV parameters. (A), (C), and (E) show the excess chemical potential for Ca^{2+}, while (B), (D), and (F) are for Mg^{2+}. The respective ions in (A) and (B) have 5 chelating oxygens, (C) and (D) have 6 chelating oxygens, and (E) and (F) have 7 chelating oxygens fixed in the binding site. Warmer colors correspond to more positive chemical potentials, while cooler colors correspond to more negative chemical potentials.
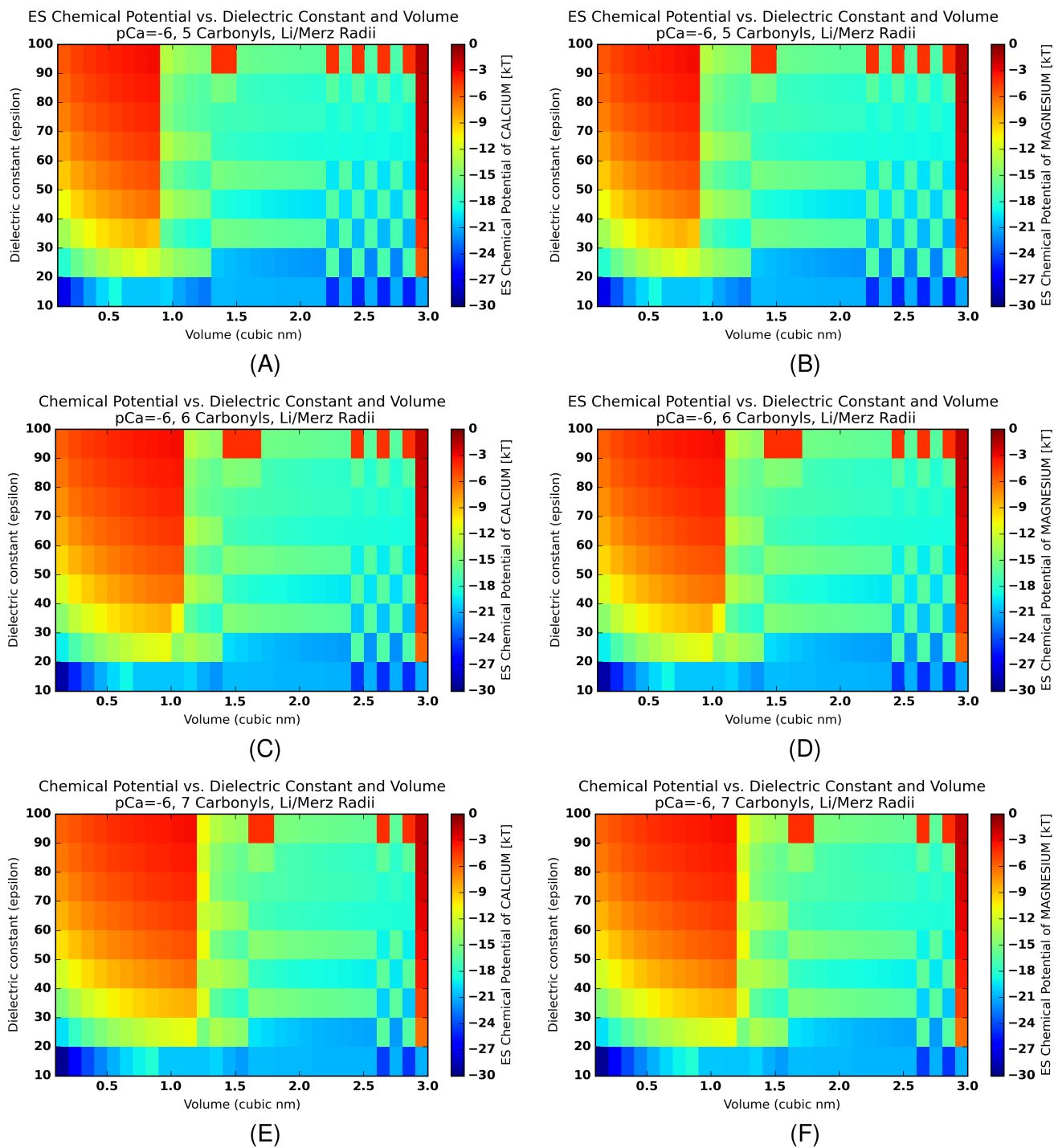
Figure S2: Electrostatic contributions to the excess chemical potential of ionic species using radii from Li/Merz and PV parameters. (A), (C), and (E) show the excess chemical potential for Ca^{2+}, while plots (B), (D), and (F) are for Mg^{2+}. The respective ions in (A) and (B) have 5 chelating oxygens, (C) and (D) have 6 chelating oxygens, and (E) and (F) have 7 chelating oxygens fixed in the binding site. Warmer colors correspond to more positive chemical potentials, while cooler colors correspond to more negative chemical potentials.
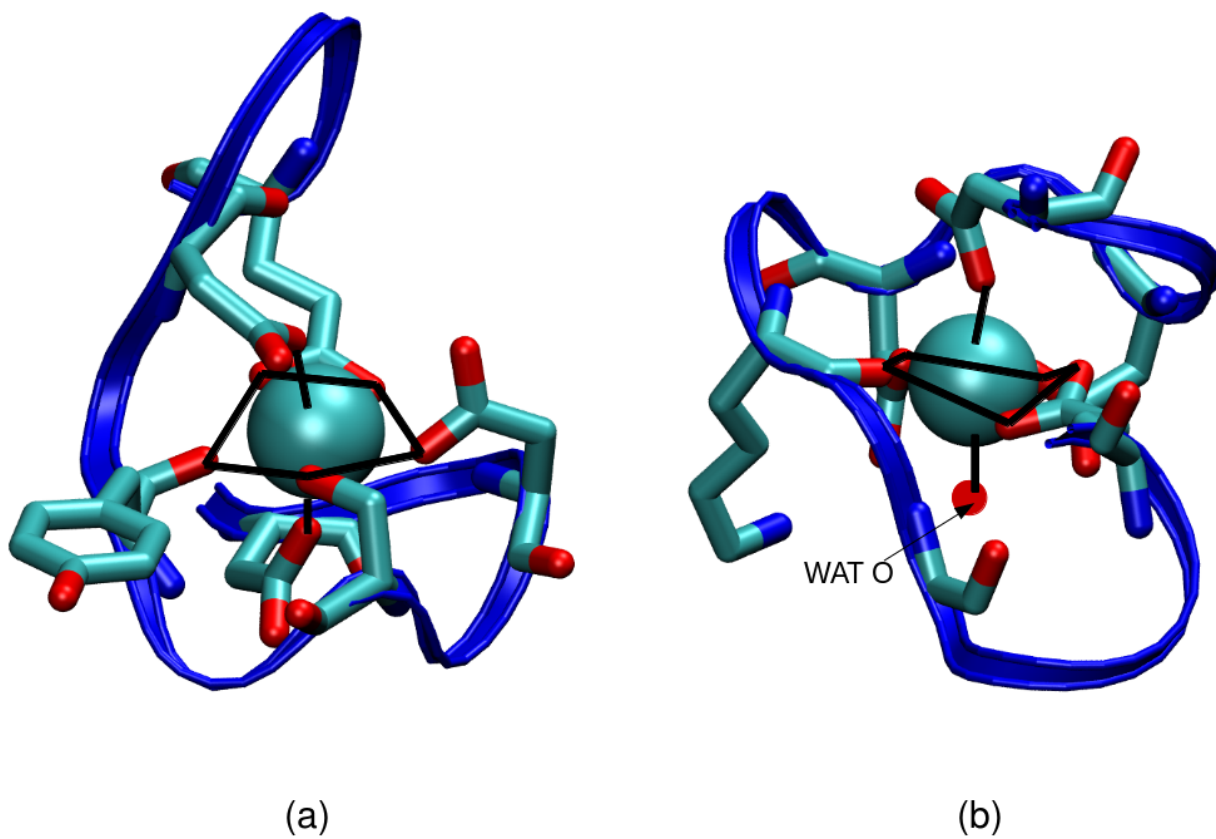
Figure S3: Licorice rendition of the L_{CD} (a) and L_{EF} (b) with Ca^{2+} bound in the pentagonal bipyramidal coordination geometry.
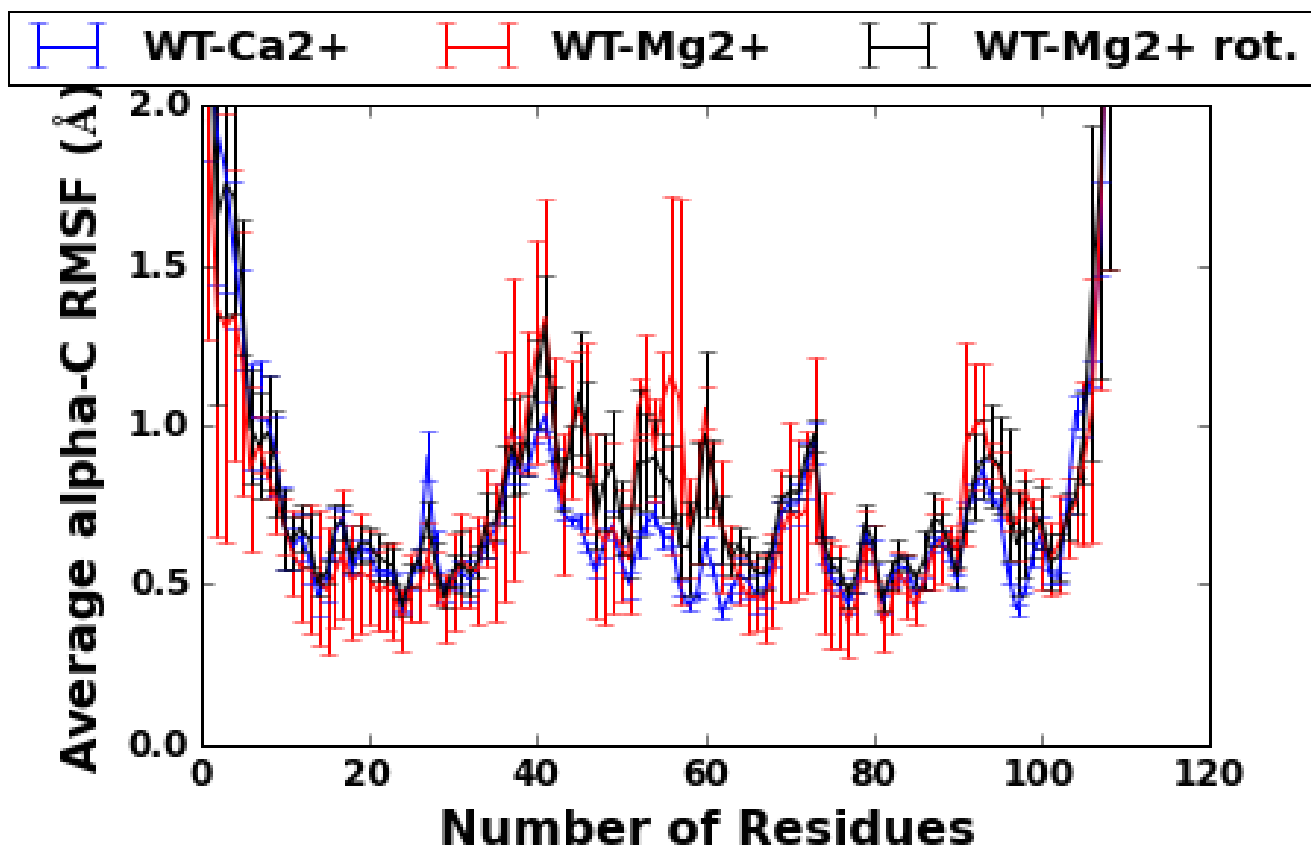
Figure S4: C_α RMSF for the PV protein bound to Ca^{2+} ('WT-Ca^{2+},' blue), Mg^{2+} using the Mg^{2+} -bound crystal (PDB code, 4PAL[9]) residue rotamers ('WT-Mg^{2+},' red), or Mg^{2+} using the twelfth position's glutamic acid monodentate rotamer selected with Chimera software ('WT-Mg^{2+} rot.,'black). RMSFs are averaged over triplicate runs.
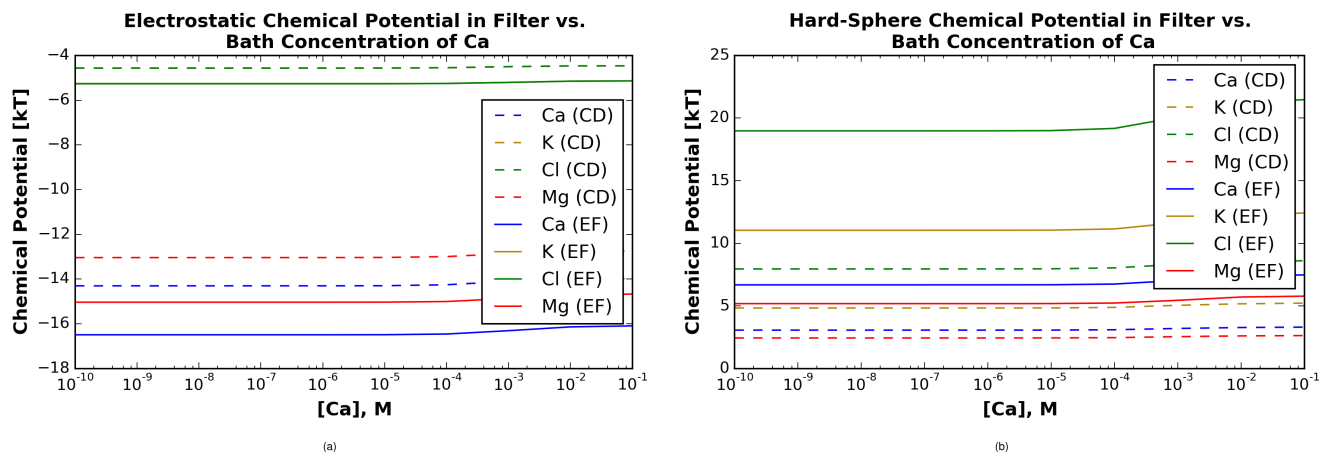
Figure S5: Electrostatic (a) and hard-sphere components (b) of the excess chemical potentials of the Ca^{2+} (blue), K$^+$ (gold), Cl$^-$ (green), and Mg^{2+} (red) ions calculated from the MSA model. Dashed lines are for the L$_{CD}$ while solid lines are for the L$_{EF}$.
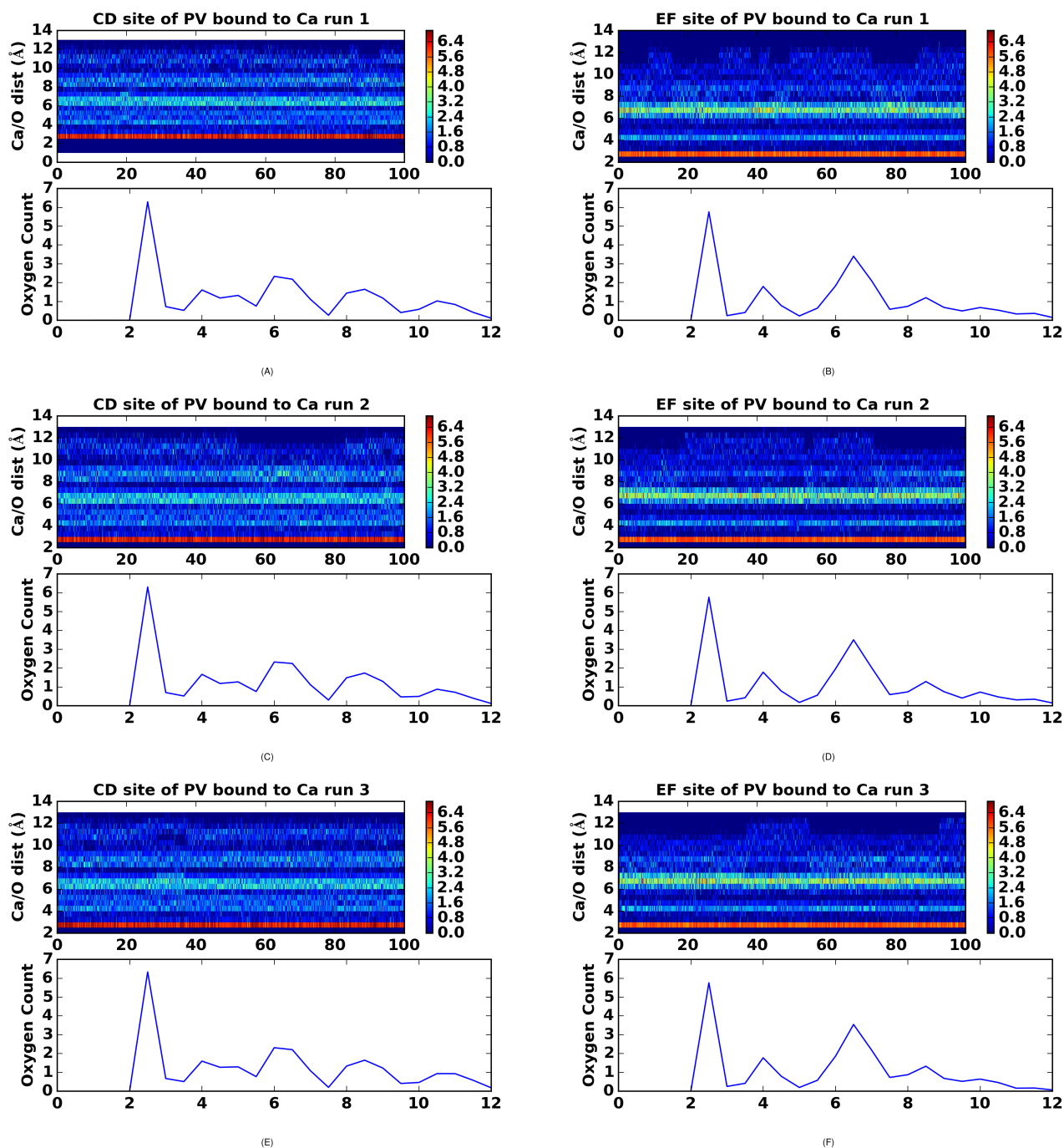
Figure S6: Oxygen density around Ca^{2+} with respect to time (top), as well as the time-averaged RDFs for each run. Warmer colors in the top portion of the plots indicate high oxygen density, while cooler colors indicate low oxygen density.
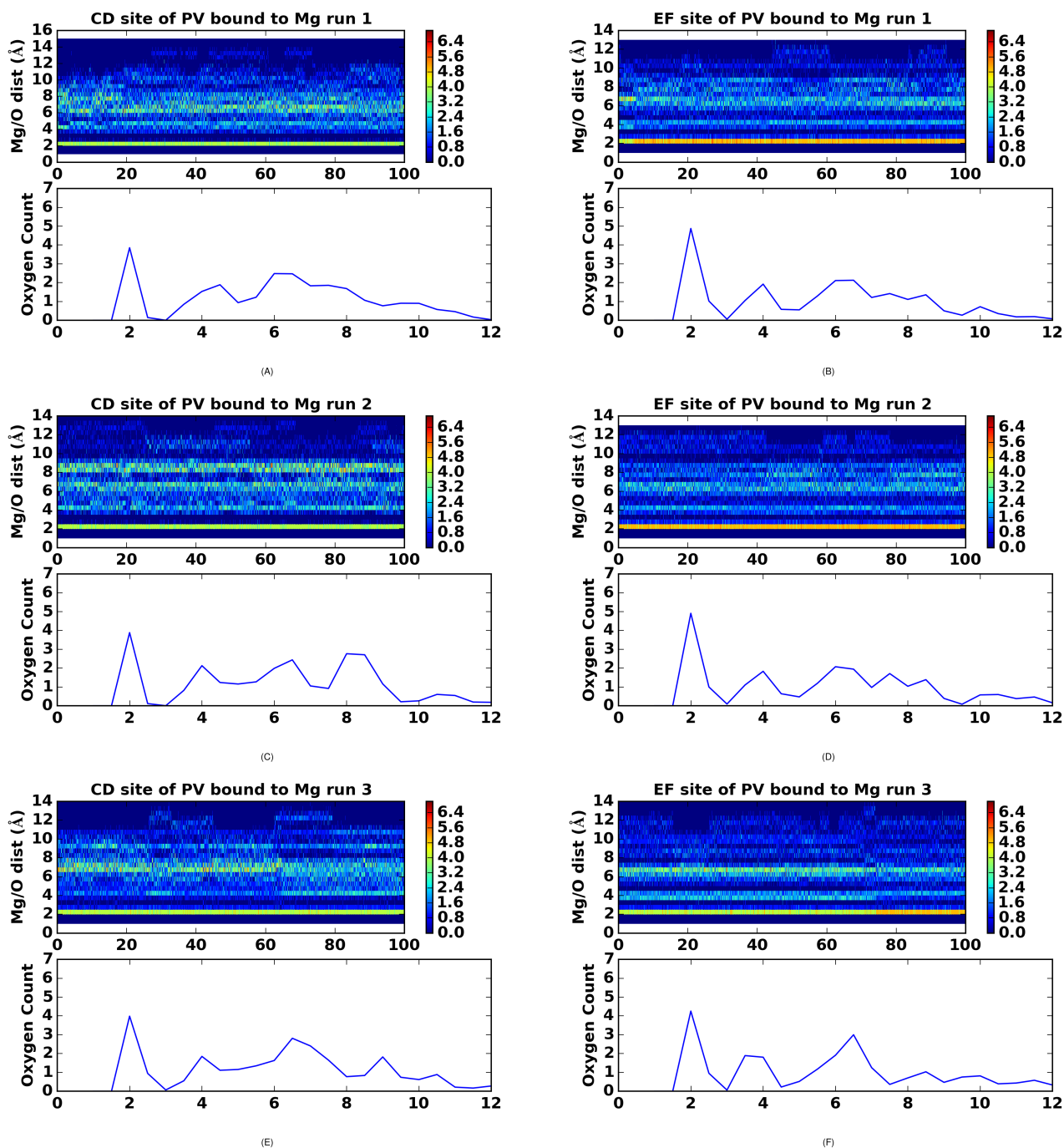
Figure S7: Oxygen density around Mg^{2+} with respect to time (top), as well as the time-averaged RDFs for each run. Warmer colors in the top portion of the plots indicate high oxygen density, while cooler colors indicate low oxygen density.
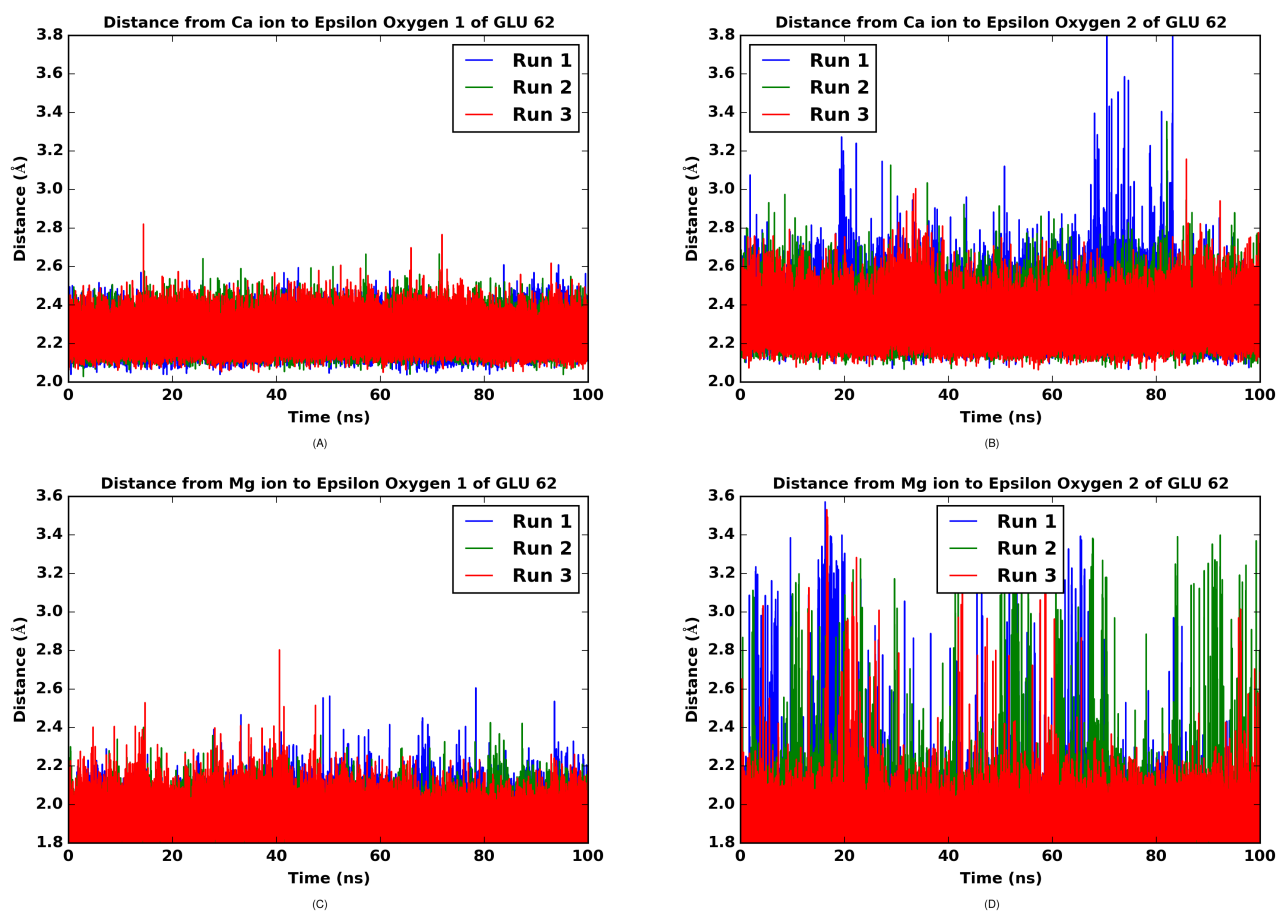
Figure S8: (A) and (B) show the distance between the epsilon oxygens of E62 and Ca^{2+}. (C) and (D) show the distance between the epsilon oxygens of E62 and Mg^{2+}. Each color corresponds to a single, 100 ns MD production run.
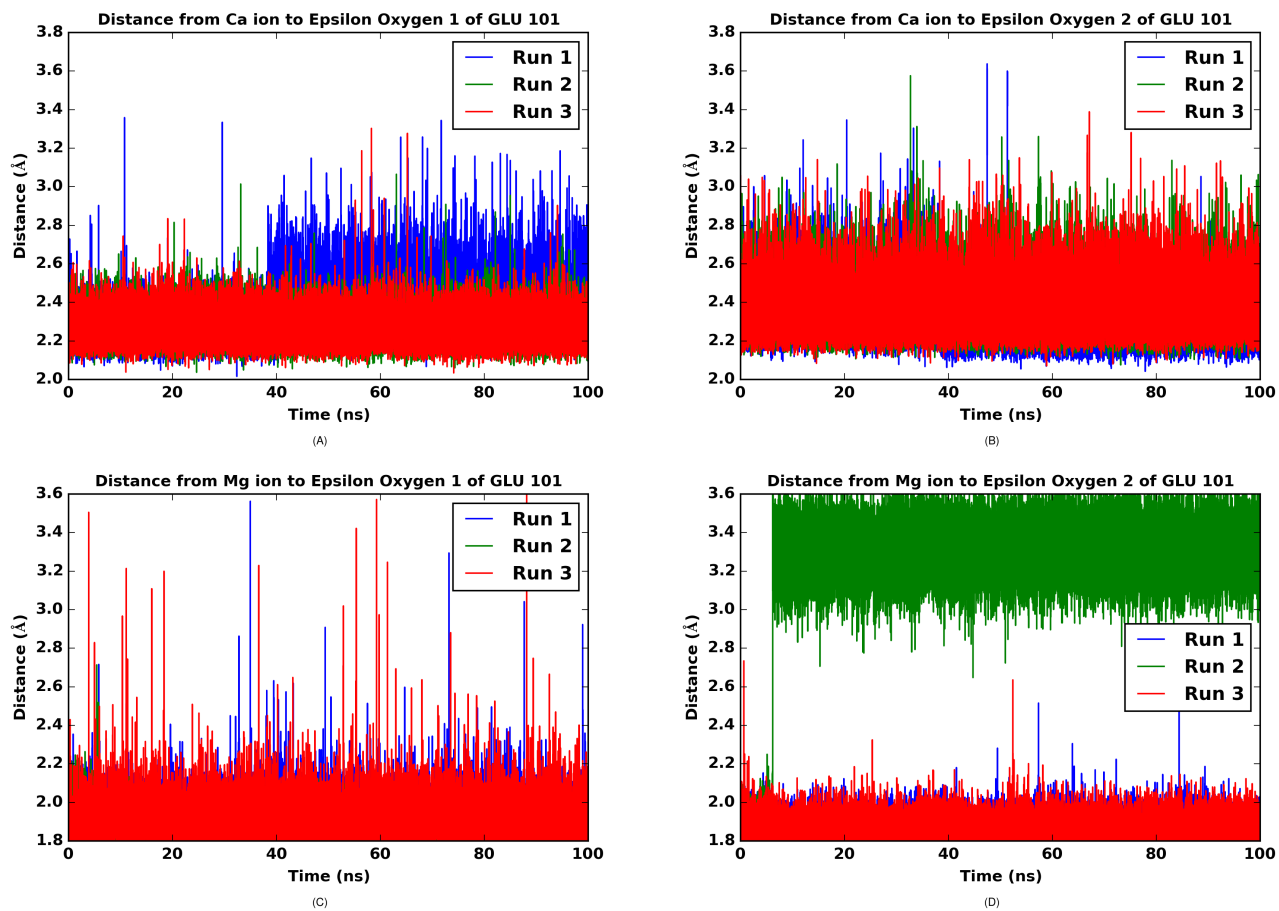
Figure S9: (A) and (B) show the distance between the epsilon oxygens of E101 and Ca²⁺. Each color corresponds to a single, 100 ns MD production run.
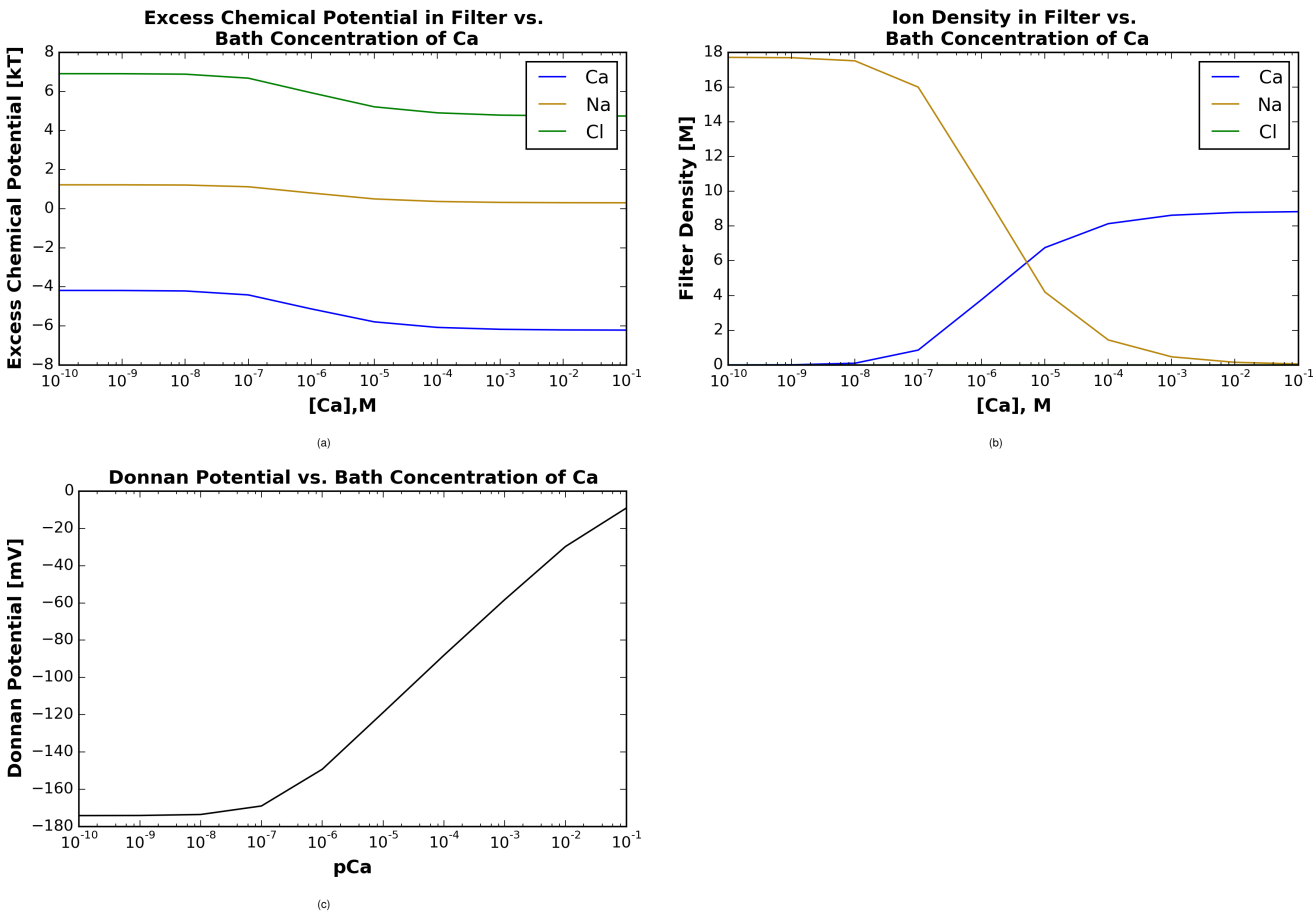
Figure S10: MSA validation plots using parameters from Nonner et al.[88] (100 mM NaCl, 8 carbonyl oxygens with a charge of -0.5e, filter volume of 0.375 nm^3, filter dielectric of 63.5, bulk dielectric of 78.4, Na$^+$ diameter of 0.204 nm, Cl$^-$ diameter of 0.362 nm, Ca^{2+} diameter of 0.200 nm, and O$^{-0.5}$ diameter of 0.278 nm). (a) shows the excess chemical potential of each ion in the system with respect to [CaCl$_2$]. (b) shows the ion filter density with respect to [CaCl$_2$]. (c) shows the Donnan Potential of the system with respect to [CaCl$_2$]. Green, gold, and blue are used to indicate chemical potentials and filter densities for Cl$^-$, Na$^+$, and Ca^{2+}, respectively. These figures agree with those from Nonner et al.[88]

(a)

(b)

(c)

(d)
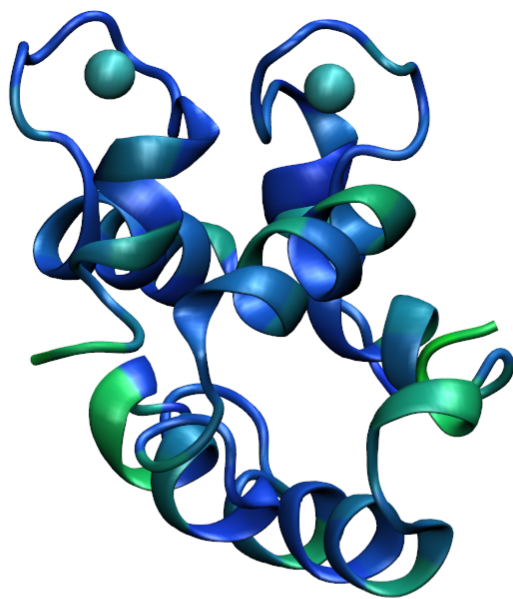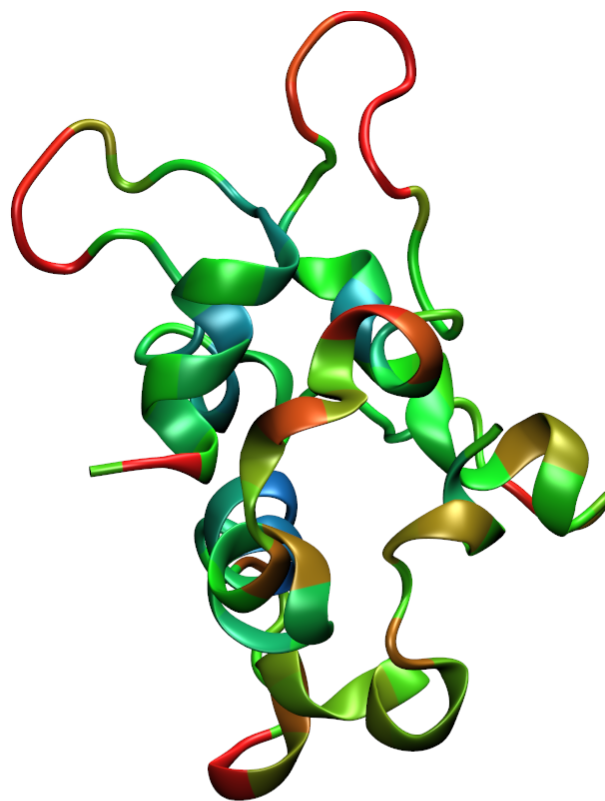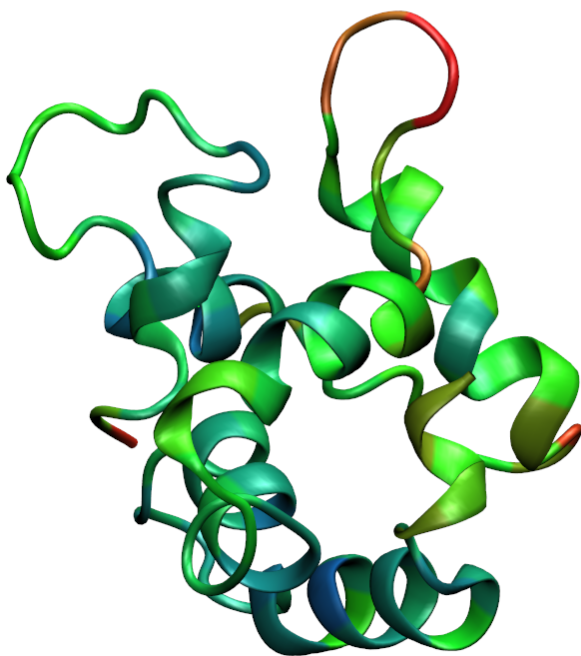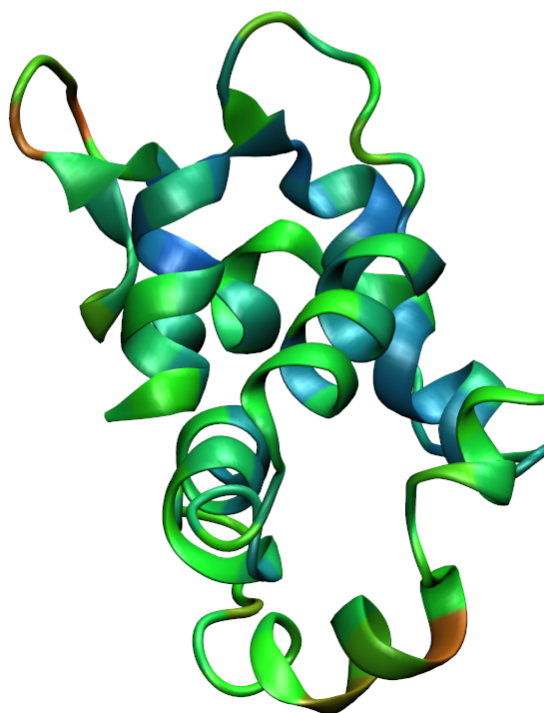
Figure S11: C$_\alpha$ RMSFs of Ca^{2+}-bound PV (a) and apo PV (b, c, and d). The minumum RMSF (dark blue) shown is 1.0 Å, while the maximum RMSF (red) shown is 8.0 Å.
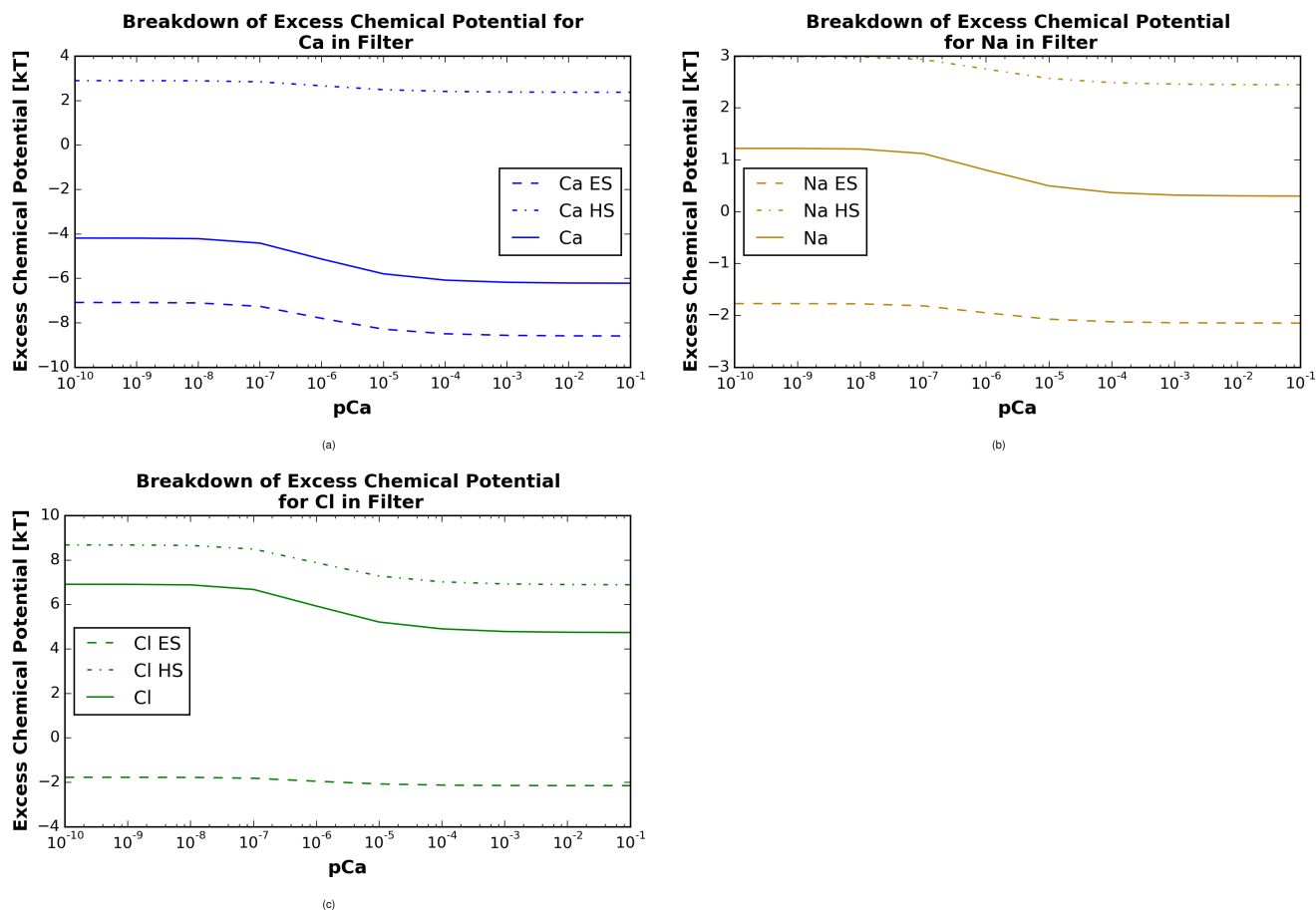
Figure S12: Hard-sphere (dotted lines) and electrostatic (dashed lines) components of the chemical potential using parameters from Nonner et al.[88] (100mM NaCl, 8 carbonyl oxygens with a charge of -0.5e, filter volume of 0.375 nm^3, filter dielectric of 63.5, bulk dielectric of 78.4, Na$^+$ diameter of 0.204 nm, Cl$^-$ diameter of 0.362 nm, Ca^{2+} diameter of 0.200 nm, and O$^{-0.5}$ diameter of 0.278 nm) for Ca^{2+} (a), Na$^+$ (b), and Cl$^-$ (c). These figures agree with those from Nonner et al.[88]
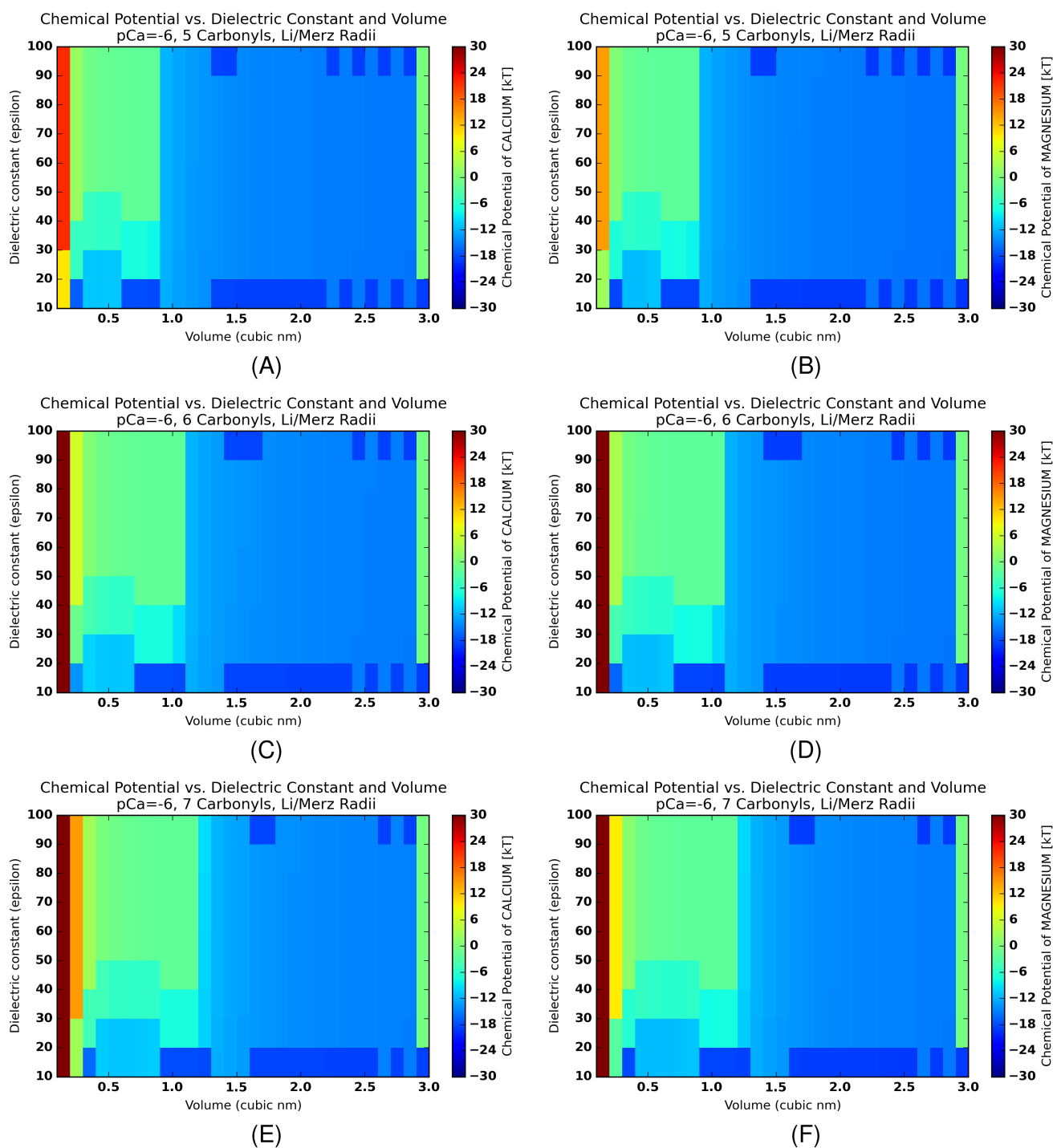
Figure S13: 2D plot depicting chemical potential for filter dielectric constants and volumes at a constant 1 μM bulk Ca^{2+} concentration. The respective filters in (A) and (B) have 5 oxygens, (C) and (D) have 6 oxygens, and (E) and (F) have 7 oxygens chelating with Ca^{2+} (A, C, and E) or Mg^{2+} (B, D, and F). Warmer colors reflect more positive chemical potentials, while cooler colors reflect more negative chemical potentials.
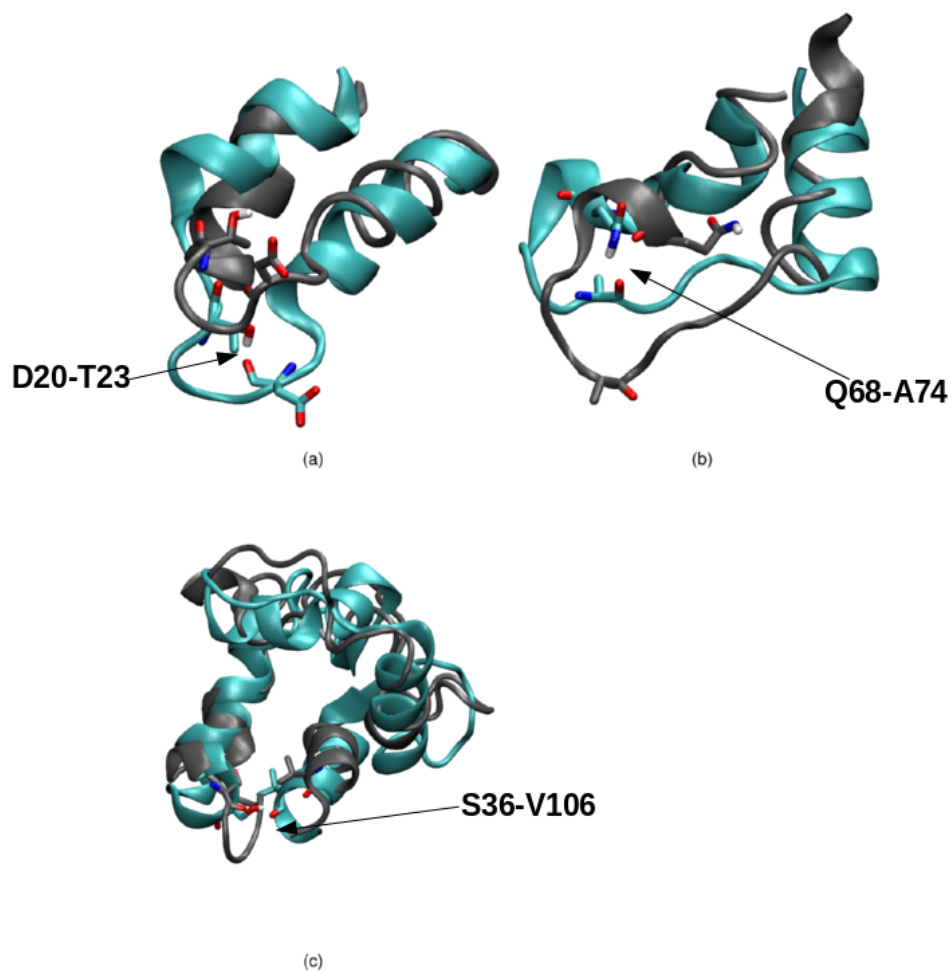
Figure S14: Notable contacts formed in the holo state, as determined from contact plot maps shown in Fig. 6. The holo state is represented by blue helices/loops, while the apo state is represented by gray helices/loops. All contacts formed are hydrogen bonding interactions. (a) shows a contact between D20 and T23, (b) shows a contact between Q68 and A74, and (c) shows a contact between S36 and V102.
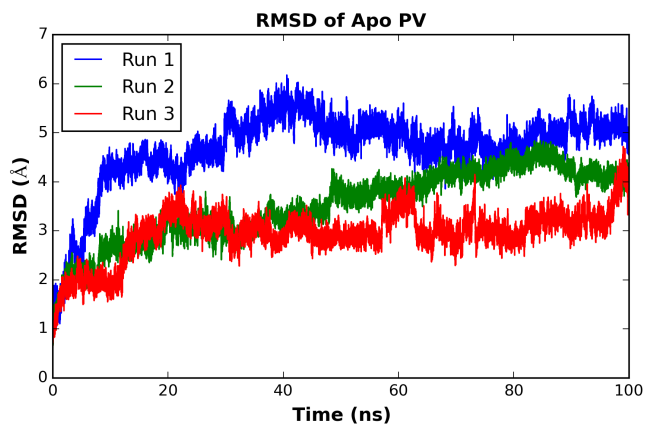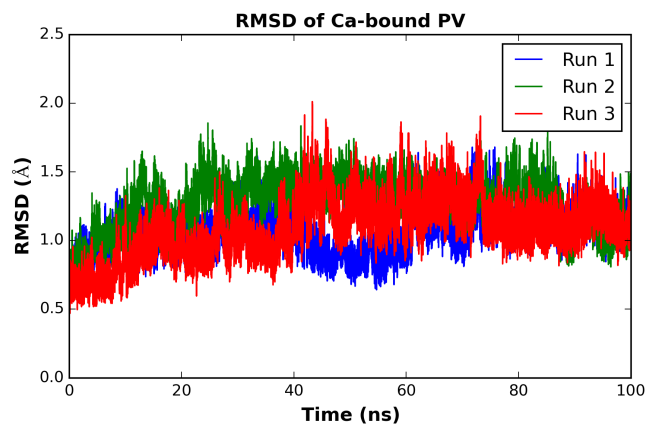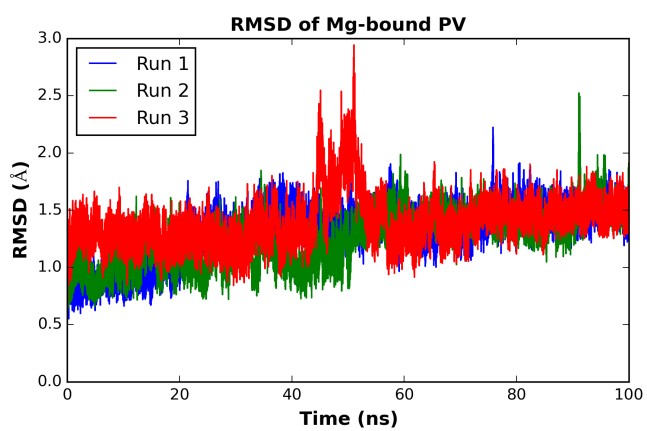
Figure S15: C_α RMSD values for the entire apo (a), Ca^{2+}-bound (b), and Mg^{2+}-bound (c) β-PV. Colors correspond to single, 100 ns MD production runs.
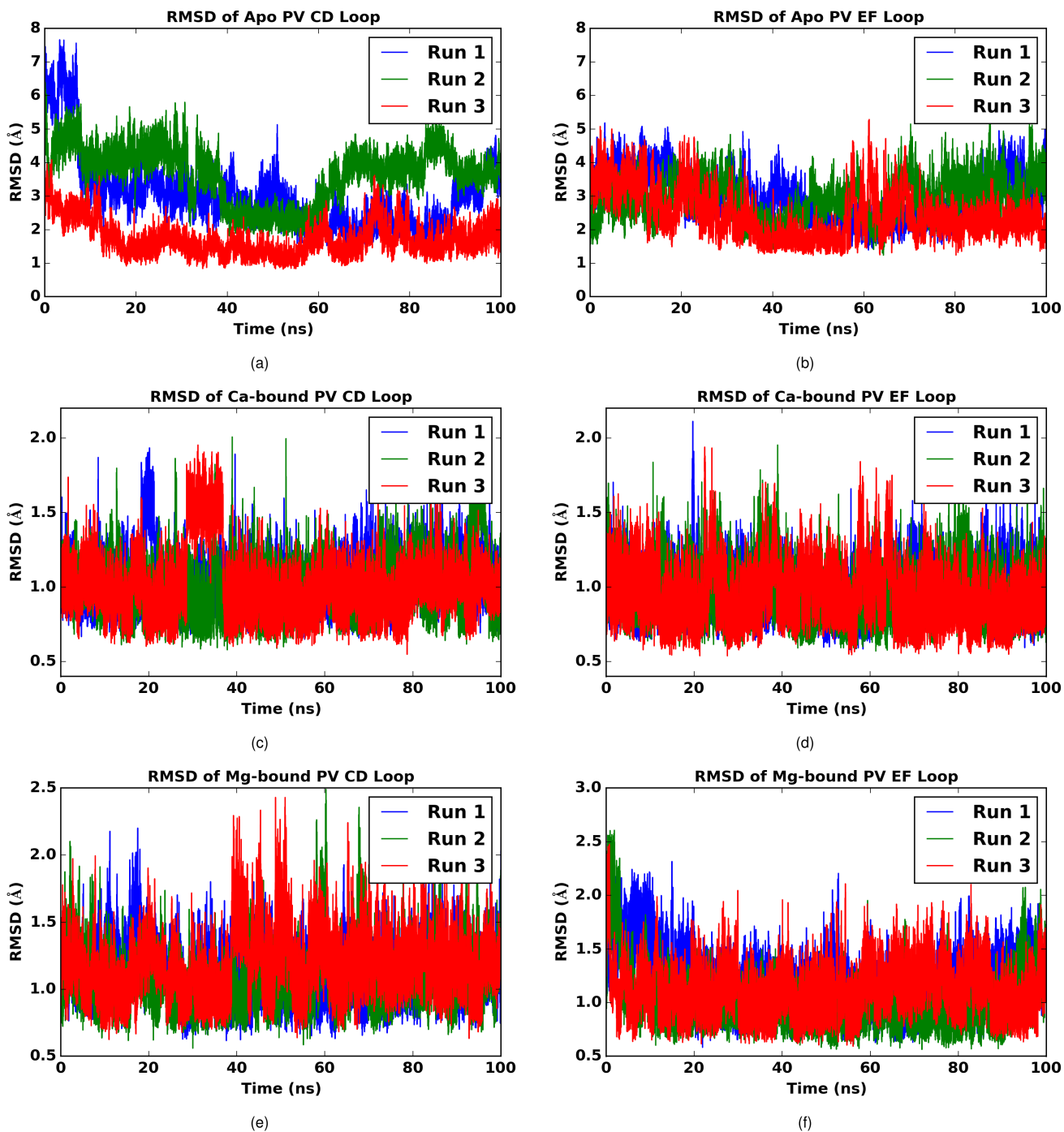
Figure S16: C_α RMSD values for the L_{CD} [(a), (c), and (e)] and for the L_{CD} [(b), (d), and (f)] of the apo (a, b), Ca^{2+}-bound (c, d) and Mg^{2+}-bound (e, f) β-PV. Colors correspond to single, 100 ns MD production runs.

Supplementary Tables

Table S1: Rat β-PV domain definitions.

Region	Residues
Helix A (H_A)	E9-C18
H_B	Q27-G34
H_C	S41-D51
H_D	E62-Y65
CD Hand (L_{CD})	D51-E62
H_E	S80-D90
L_{EF} Hand	D90-E101
H_F	D100-H107